On the combined use of Vortex Generators and Gurney Flaps for turbine airfoils

L Chng[1], J Alber[2], D Ntouras[3], G Papadakis[3], N Kaufmann[4], P Ouro[1,5], M Manolesos[6,7]

[1]Cardiff University, Cardiff, CF10 3AT, UK
[2]Technische Universität (TU) Berlin, Müller-Breslau-Str. 8, 10623 Berlin, Germany
[3]National Technical University of Athens, Iroon Politechniou 9, 15780, Greece
[4]Sustainable Marine, Edinburgh, EH6 6QW, UK
[5]The University of Manchester, Manchester, M13 9PL, UK
[6]City, University of London, London EC1V 0HB, UK
[7]Swansea University, Swansea, SA1 0NB, UK

Abstract. While Vortex Generators (VGs) and Gurney Flaps (GFs) are commonly used for airfoil flow control, studies of a combination of the two devices are rare. The present investigation aims at examining the combined effect of VGs and GFs on a 20% thick airfoil. To this end, a wind tunnel investigation coupled with a computational study was performed. The present paper presents force, pressure and Stereo Particle Image Velocimetry measurements, along with Unsteady Reynolds Averaged Navier Stokes simulations.

1 Introduction

Vortex Generators (VGs) are already a commercialized retrofit for large rotor blades. They are usually located in the root region in order to reduce the amount of separated flow, or further outboard, to counteract the effects of increased leading-edge roughness. They generate streamwise vortices, which energize the boundary layer (BL) and help it withstand the adverse pressure gradient for longer. There is a large number of experimental and numerical studies showcasing their effectiveness on flow control for profiles and blades, e.g. (1–4).

Gurney Flaps (GFs) are more widely known for their use in the motorsport industry but have shown promising results for wind turbine applications (5). They consist of a thin strip, extending parallel to the trailing edge, normal to the pressure side. Their presence modifies the flow circulation around the airfoil shifting the Kutta condition, increasing both lift and drag. A recent study (6) demonstrated that so-called mini-GFs with a height of approximately 25%c of the local BL led to an increase in both lift and drag in such a way that the lift to drag (L/D) ratio is also improved. This is in agreement with a relevant review which highlighted that very small GF heights provide higher benefits in terms of the L/D ratio (7).

Despite the considerable amount of literature on each of the devices, research on the interaction of VGs and GFs is less profound. One earlier study (8) illustrated that maximum lift can be increased by 36% by combining VGs with a GF. However, it was found that the severe drag penalty led to a reduction of the L/D performance. A more recent study (6) investigated a combination of mini-GFs with VGs leading to an improved L/D ratio.

The purpose of the present research is to examine the combined effect of the two passive flow control devices in detail. To this end a combined experimental and computational study was performed. The remaining of this paper is organised as follows. First the methodology of the investigation is described, then the results are presented and discussed and the paper closes with the presentation of the main conclusions.

2 Methods

2.1 Experimental Set-up

All experiments were conducted at the low-speed wind tunnel at Swansea University. The profile tested was a 20% thick airfoil which spanned vertically across the wind tunnel's test section. The airfoil profile chord length,

c, was 0.5 m and the Re number was 1.0×10^6. Force, pressure, and Stereo Particle Image Velocimetry (PIV) measurements are reported in this paper. The experiments were conducted under both free and fixed transition conditions, except for the Stereo PIV, which was under fixed transition conditions only. To fix transition, a 0.26mm thick zigzag tape was applied across the span on the suction and pressure sides at chordwise positions, 5%c and 10%c, respectively. Wind tunnel corrections for bodies spanning the tunnel test section were applied (9).

The wing model was supported on two strain-gauge-based AMTI MC12-1000 six-axis force balances, measuring simultaneously with a sampling rate of 300 Hz for 30 seconds. Surface pressure measurements were taken from the 63 pressure taps around the airfoil's surface, which were used to calculate the profile lift. Pressure measurements were also taken 1.8 chords downstream from the model using a wake rake of 60 total pressure tubes and 3 static pressure probes. The wake rake data were used to calculate the profile drag (9). Both pressure measurements were performed at a sampling rate of 10 Hz for 30 seconds.

Image acquisition for the Stereo PIV measurements was performed by means of two 5.5 Mpixel sCMOS double-shutter cameras located outside the wind tunnel test section. A double pulse 200mJ ND:YAG laser was used with a wavelength of 532 nm, which was operating at a frequency of 0.1 Hz with a pulse separation time of 32µs. For each configuration, a total of 1750 images were acquired and the interrogation area was 64x64 pixel with 50% overlapping. The Stereo PIV measurement plane was normal to the flow and parallel to the wing span, 5.8%c downstream of the trailing edge, as illustrated in Figure 1. The plane location was selected so that both the streamwise vortices from the VGs and the spanwise vortices shed form the GF were captured.

The airfoil was at $\alpha = 6°$, which was the design angle for the specific profile, and is a section from SCHOTTEL's SIT250 tidal turbine blade (10). The coordinates of the profile are confidential, but this does not affect the generality of the findings. In Figure 1 is a generic cambered airfoil profile, similar to the one tested, is illustrated.

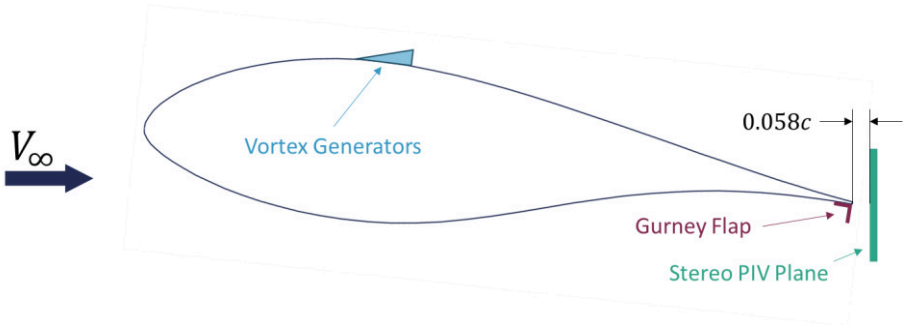

Figure 1. Schematic of the PIV plane in relation to a generic airfoil model, positioned at $\alpha = 6°$. The flow control devices (Vortex Generators and Gurney Flap) are also shown, not to scale.

2.2 Flow Control Devices

Prior to the present study, a VG parametric investigation (11) was performed and the best performing configuration was used for this research. Triangular counter rotating VGs with a height of $h = 0.7\%c$ were found to increase maximum L/D by 20.8% in (11). The VG parameters are defined in Figure 2 and the relevant values are given in Table 1. The VG devices were 3D printed with a baseplate of 0.5mm thickness.

Table 1. Vortex Generator geometrical parameters

Parameter	**h**	**D**	**d**	**L**	**x**
Definition	VG height	VG pair distance	VG distance within pair	VG length	VG Chordwise location
Value	0.7c	7h	3.5h	3h	30%c

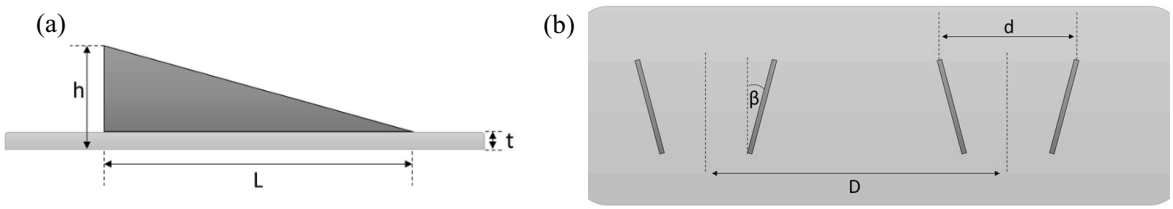

Figure 2. Vortex Generator parameters. (a) Side view; (b) Top view (flow coming from the bottom).

For the present study, the VGs were combined with three different GF sizes, of 0.4%c, 0.8%c and 1.2%c. The GFs were 90° angle profiles made of brass, located on the airfoil pressure side at the trailing edge, see also Figure 1. XFOIL (12) simulations were used to estimate the boundary layer height at the position of the flow control devices for both fixed and free transition conditions and the relative height for each device is given in Table 2.

Table 2. Size of flow control devices with respect to chord length and local boundary layer height based on XFOIL calculations at AoA = 6°

Device	Height (%c)	Fixed Transition (%δ)	Free Transition (%δ)
3.5mm VGs	0.7	43	85
2 mm GF	0.4	10	12
4 mm GF	0.8	20	25
6 mm GF	1.2	31	37

2.3 Numerical Approach

For the numerical part of the investigation, MaPFlow (13), an in-house unsteady Reynolds-Averaged Navier Stokes (URANS) solver with VG modelling capabilities (4). MaPFlow, which was primarily developed at the National Technical University of Athens, is a cell centred CFD Solver that can use both structured and unstructured grids. It is capable of solving compressible and fully incompressible flows using the artificial compressibility method (14). Additionally, incompressible flows with small compressibility effects are feasible using Low Mach Preconditioning (15). In all cases, the convective fluxes are discretized using the approximate Riemann solver of Roe (16). For the reconstruction of the flow field a 2nd order piecewise linear interpolation scheme is used. The Venkatakrishnan limiter(17) is utilized when needed (e.g. in cases of shock waves). The viscous fluxes are discretized using a central 2nd order scheme. Turbulence closures implemented on MaPFlow include the one equation turbulence model of Spalart and Allmaras (SA) (18) as well as the two-equation turbulence model of Menter (k-ω SST)(19).

In this approach, the flow is treated as fully incompressible. The governing equations are presented in Eq. (1) . The system of equations, in 3 dimensions, consists of 4 scalar equations. The equations are augmented by the pseudo-time derivatives of the variables. The aim of the numerical procedure is to drive these derivatives to zero; thus the original unsteady system of equations will be retrieved. The coupling of the equations is performed during the pseudo-time, where a relation between the density and the pressure field is assumed. The coupling is controlled through the relation $\frac{\partial \rho}{\partial p}|_{\tau} = \frac{1}{\beta}$, where β is a free parameter.

$$\Gamma \int_{\Omega} \frac{\partial \vec{Q}}{\partial \tau} d\Omega + \Gamma_e \int_{\Omega} \frac{\partial \vec{Q}}{\partial t} d\Omega + \int_{\partial\Omega} \left(\vec{F}_c - \vec{F}_v\right) dS = \int_{\Omega} \vec{S}_q d\Omega \qquad (1)$$

In the above, Ω is a control volume with boundary $\partial\Omega$, $\vec{Q} = [p, \vec{u}]^T$ is the vector of the unknown variables (pressure p ,velocity $\vec{u}$), vector $\vec{S}_q$ contains the various source terms of the equations (such as the BAY model for the vortex generators), while t and τ denote the real and fictitious time, respectively. Finally, $\vec{F}_c$ is the vector of the convective fluxes and $\vec{F}_v$ the vector of the viscous fluxes. The two vectors are given in Eq. (2). By ΔV the velocity difference between the contravariant velocity $V_n = \vec{u} \cdot \vec{n}$ and the grid face velocity due to the mesh motion $V_g = \vec{u}_{vol} \cdot \vec{n}$ is denoted. In the present study the mesh was stationary; thus, $V_g = 0$.

$$F_c = \begin{bmatrix} V_n \\ u\Delta V + pn_x \\ \rho v \Delta V + pn_y \\ \rho w \Delta V + pn_z \end{bmatrix}, \; F_v = \begin{bmatrix} 0 \\ \tau_{xx}n_x + \tau_{xy}n_y + \tau_{xz}n_z \\ \tau_{yx}n_x + \tau_{yy}n_y + \tau_{yz}n_z \\ \tau_{zx}n_x + \tau_{zy}n_y + \tau_{zz}n_z \end{bmatrix} \qquad (2)$$

Furthermore, the viscous fluxes are computed through the viscous stresses τ_{ij}, which in turn are expressed using the Boussinesq approximation in Eq. (3) :

$$\tau_{ij} = (\mu_t + \mu)\left(\frac{\partial u_i}{\partial x_j} + \frac{\partial u_j}{\partial x_i}\right) - \frac{2}{3}\rho k \delta_{ij} \qquad (3)$$

where, μ is the viscosity of the fluid, μ_t is the turbulent viscosity, k the turbulent kinetic energy and δ_{ij} the Kronecker's delta.

Regarding the vortex generator modelling the jBAY model (20) is employed following the guidelines presented in (4). The total force acting on the fluid is:

$$\vec{L} = \sum \vec{L}_i \quad (4)$$

where $\vec{L}_i$ is the source term added to the momentum equations at the cells where the model is applied. $\vec{L}_i$ is given by Eq. (5)

$$\vec{L}_i = c_{VG} S_{VG} \frac{V_i}{\sum V_i} \rho |\vec{u}|^2 (\hat{u} \cdot \hat{n}) \left(\hat{u} \times \hat{b}\right) (\hat{u} \cdot \hat{t}) \quad (5)$$

where c_{VG} is the BAY model constant, V_i is the grid cell volume and $\hat{n},\ \hat{b},\ \hat{t}$ are the VG surface unit vectors. The constant c_{VG} is the only model parameter and acts as a relaxation parameter, controlling the strength of the force term. In this work the constant was defined as $c_{VG} = 10$. In its jBAY variation, which is an elegant simplification of the model, the source term is only applied to the cells engulfing the VG geometry, as first described in (20).

Grid and Timestep Independency

Prior to presenting the comparison between the simulations and the experimental data a grid and time independency study is conducted. Both the grid and time independence study are presented for the baseline airfoil with the gurney flap attached. Three successively refined grids consisting of 63000 cells (Coarse), 114000 cells (Medium) and 234000 cells (Fine) are generated. Comparison between the grids for the three meshes is presented in Figure 3 (a) for the drag coefficient (Cd) for various angle of attacks (AoA) up to 10^0. Evidently, the difference between the coarse and the fine grid is relatively large while the medium and the fine mesh are in very good agreement. Consequently, the medium mesh is employed for the rest of the study.

Using the medium mesh, the time step independence study is presented in Figure 3 (b). Again, Cd is compared for three different time-steps, namely $dt = 5.0 \cdot 10^{-04}, 2.5 \cdot 10^{-04}$ and $1 \cdot 10^{-04}$. It is evident, that the agreement up to AoA=10^0 is very good for all three timesteps. However, at AoA=12^0 differences start to emerge due to the onset of separation. Nevertheless, only marginal differences are observed between the two finer timesteps and thus $dt = 2.5 \cdot 10^{-04}$ is employed for the rest of the work.

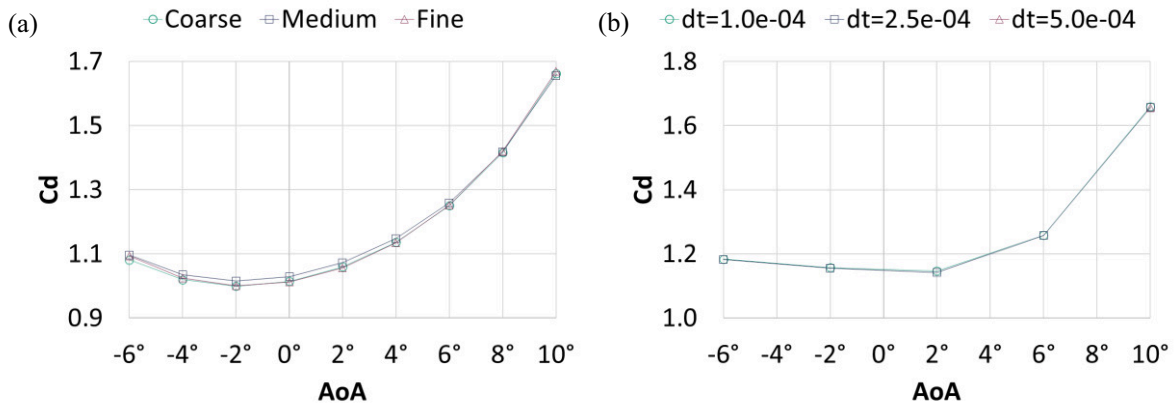

Figure 3. Comparison of the drag coefficient (a) for three successively refined meshes and (b) for three different time-steps. URANS data at $Re = 10^6$, normalised results.

3 Results

Pressure Measurements – Fixed Transition

The effect of GF height on the baseline airfoil performance under fixed transition is given in Figure 4. All GF heights lead to an increase in lift and drag values compared to the baseline. Figure 5 shows the effect of VGs on the baseline airfoil and the effect of GFs on the airfoil with VGs. The VG effect is as expected, increasing drag at low angles of attack (AoA) and delaying the onset of stall. The effect of the GFs on the airfoil with VGs is very similar to that on the baseline airfoil, increasing both lift and drag.

Figure 6 shows the increase in drag ($\Delta Cd_{device}(a) = Cd_{device} - Cd_{baseline}$) for varying GF heights on the baseline airfoil and the airfoil with VGs. With or without the VGs, the drag increases linearly with GF height. A third curve is also plotted, showing the drag increase due to the presence of VGs ($\Delta Cd_{VG}(a = 0°) = 0.002$). The

results suggest that for the fixed transition case, the combined effect of GFs and VGs is not a simple linear superposition of the effect of VGs and the effect of GF on the baseline airfoil.

Overall, the best GF and VG combination to improve maximum L/D performance was the 0.4%c GF with an increase of 23.4%. The other GFs when combined with VGs, improved maximum L/D by 17.3% and 15.6% for 0.8%c and 1.2%c GF, respectively. The best performing VG + GF combination (VG + 0.4%c GF) is hence examined further in the remaining of this report.

At high AoA, Stall Cells appear on airfoils that experience trailing edge type of stall (21). Stall Cells are notoriously unstable (22,23) and can cause flow bifurcations. These bifurcations appear in the pressure tap measurement timeseries as sudden jumps in the pressure level (24). In the present case, this behaviour is observed just after $\alpha_{C_{l,max}}$ for all cases, as the VGs delay the formation of Stall Cells. As expected, the presence of the GF increases the magnitude of the pressure jumps, since the lift is higher for the cases with the VGs. A representative timeseries from all cases is given in Figure 8.

Numerical Results – Fixed Transition

In the interest of brevity, the CFD results are presented here in the form the predicted effect of each device on the force coefficients, $\Delta C_l = C_{l,device} - C_{l,baseline}$ and $\Delta C_d = C_{d,device} - C_{d,baseline}$. These predictions are compared in Figure 9 with the relevant measured data. The separate effect of VGs and GF on both lift and drag is predicted very well by the URANS code, especially at lower AoA. The agreement between the experiments and CFD is not equally good when the two devices are combined, which suggests that an interaction mechanism is in place that is not captured equally well by the numerical approach. For AoA beyond stall, when stall cells appear on the airfoil in the experiments, the agreement is not as good for any of the examined cases. This is expected (2,25), as the numerical approach employed in this study (low Aspect Ratio simulations) is incapable of capturing stall cells, which require a computational domain with $AR > 0.5$ (26).

Pressure Measurements – Free Transition

For completeness, the effect of the best performing combination is further examined under free transition conditions. Figure 10 shows the effect of each individual device as well as their combined effect on the baseline airfoil. In terms of lift, the effect of the VGs and the smallest GF appears to be superposed. Regarding drag, both the relative and the absolute (not shown here) increase are higher in the free transition case compared to the fixed transition case. This is as expected, given the lower baseline drag values and thinner boundary layer in the former case. For the case where VGs and GF are combined, the drag increase before stall ($-6° \leq a \leq 14°$), appears to be a linear combination of the drag increase caused by each device separately, see **Figure 7**. This contrasts with the fixed transition case, as discussed. At this moment it remains unclear why the interaction is different between the two cases, but possible causes are the state and the height of the BL when it reaches the two devices and the subsequent interaction of the VG streamwise vortices with the spanwise bluff body shedding from the GF.

Stereo PIV and CFD Results – Fixed Transition

Stereo PIV measurements for the baseline airfoil, the case with the 0.4%c GF, the VGs, and their combination is given in Figure 11. The effect of the GF is to deepen and widen, along the Y axis, the airfoil wake. At the same time, the downwash angle is increased. This agrees with the observed increase in lift and drag from the balance and pressure measurements. The VGs introduce structured three-dimensionality to the flow where the regions of upwash and downwash can be clearly identified. Overall, the wake is wider, but no increase in downwash is observed, in agreement with an increase in drag and no change in lift at this angle of attack, $\alpha = 6°$. When VGs and the GF are applied simultaneously, it appears as if the two effects are combined, as the wake is three-dimensional as in the VG case, with lower velocities and increased downwash, as in the GF case. Further analysis is expected to identify the interaction between the streamwise and spanwise vortices shed from the VGs and the GF, respectively, in terms of turbulence statistics.

Numerical predictions for the same cases are also shown in Figure 11. The effect of each case (VGs, GF, combination of the two), as described in the previous paragraph, is predicted correctly in qualitative terms. The contours appear more diffused in the experimental results compared to the simulations. This can be attributed, at least partially, to the coarser resolution of the measurement grid compared, which is 2.9 times coarser in the z-direction than that of the computational mesh.

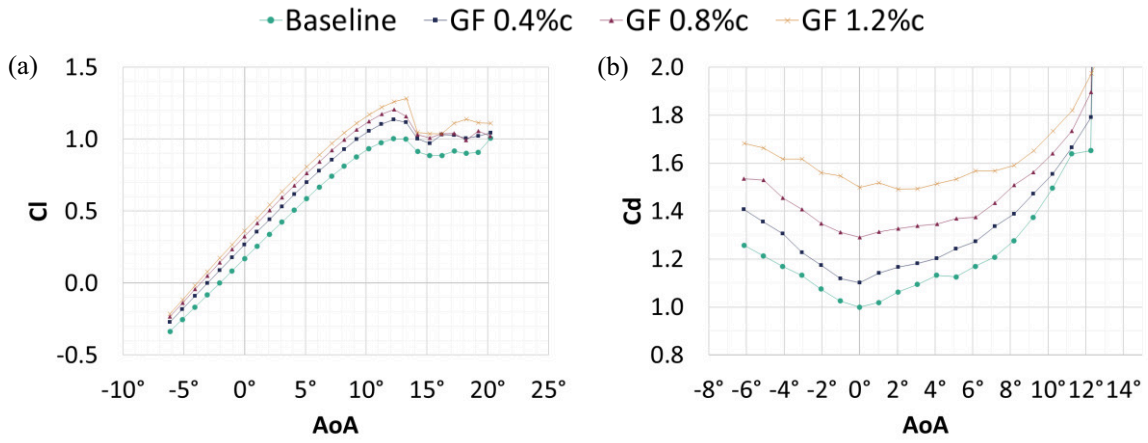

Figure 4. Lift (a) and drag (b) coefficient variation with AoA the baseline airfoil for 0.4%c, 0.8%c and 1.2%c GF heights, under fixed transition conditions. Wind Tunnel data at $Re = 10^6$, normalised results.

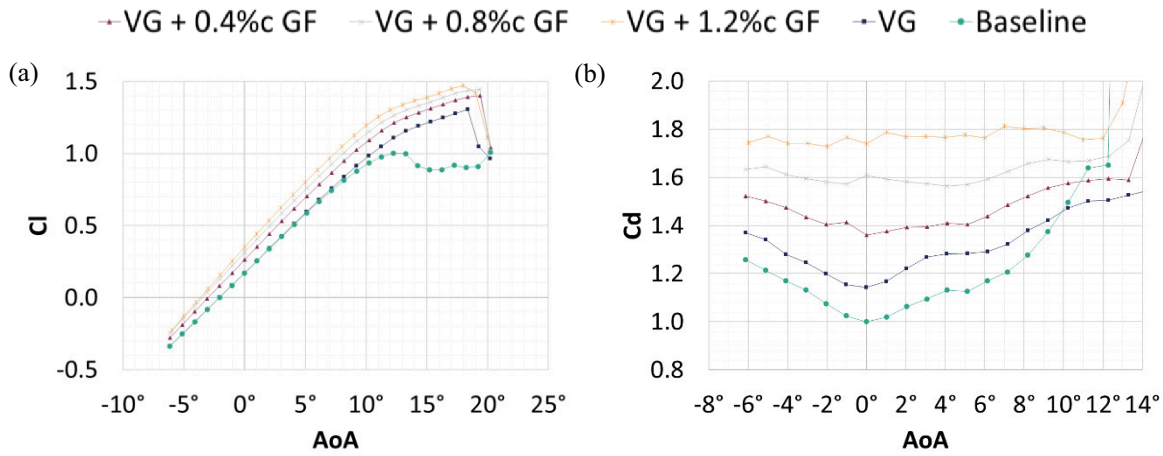

Figure 5. Lift (a) and drag (b) coefficient variation with AoA for the airfoil with Vortex Generators and 0.4%c, 0.8%c and 1.2%c GF, under fixed transition conditions. Wind Tunnel data at $Re = 10^6$, normalised results.

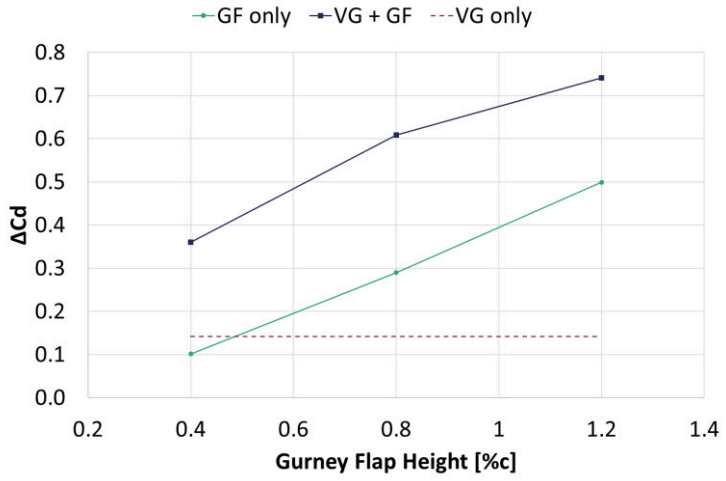

Figure 6. Drag increase for different GF heights with and without Vortex Generators under fixed transition at $\alpha = 0°$. Wind Tunnel data at $Re = 10^6$, normalised results.

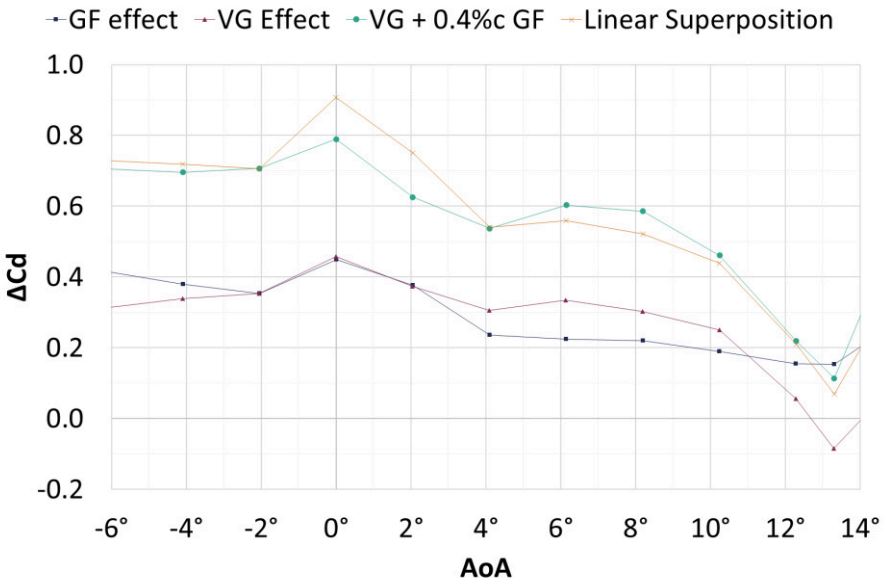

Figure 7. Drag increase for the VGs, 0.4%c GF and their combination under free transition condition. The linear superposition curve is the addition of the GF effect and VG effect curves and shows that the two effects are linearly combined. Wind Tunnel data at $Re = 10^6$, normalised results.

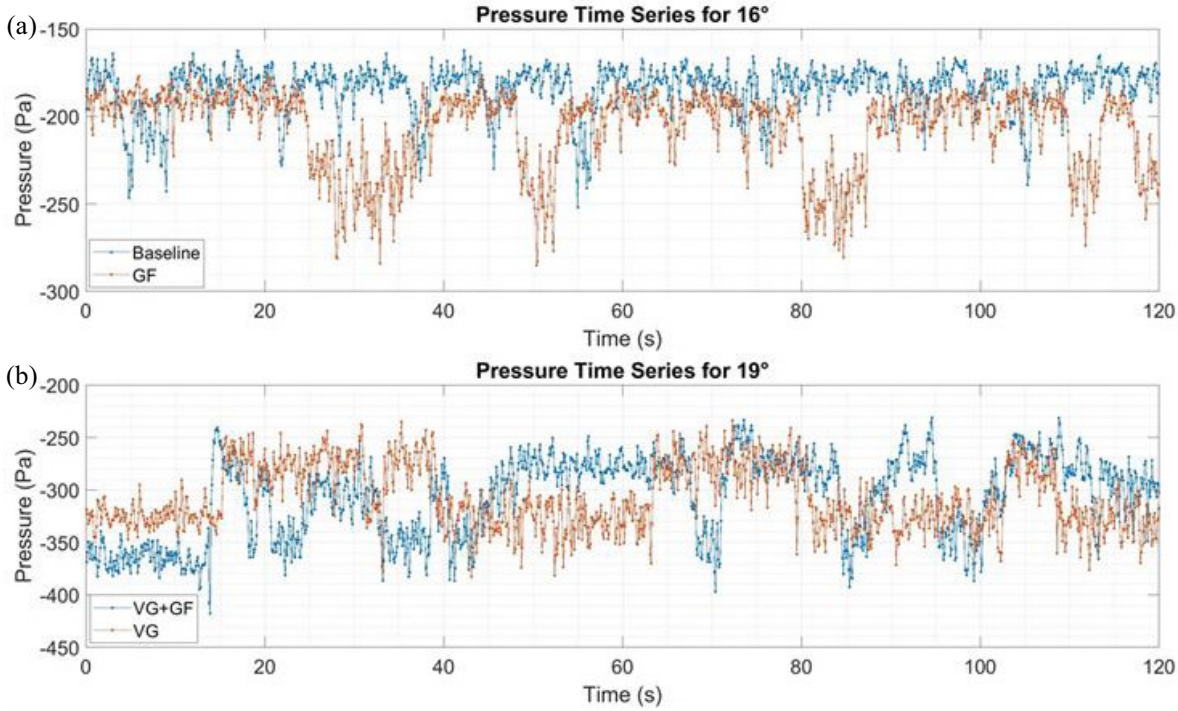

Figure 8. Pressure time series from a pressure tap on the airfoil suction side at x/c=56%. Data from (a) the baseline case and 0.4%c GF and (b) VGs and VG + 0.4%c GF combination under fixed transition conditions, at $Re = 10^6$.

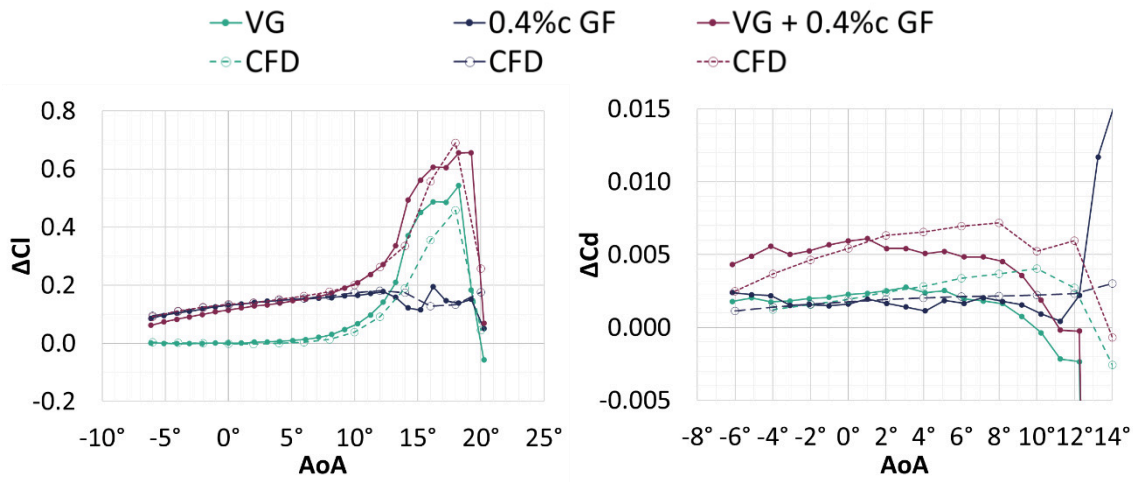

Figure 9. Effect of the Vortex Generators, the 0.4%c Gurney Flap and their combination on lift and drag for the baseline airfoil under fixed transition conditions. Comparison of experimental data (solid lines) with CFD predictions (dashed lines) at $Re = 10^6$, actual values.

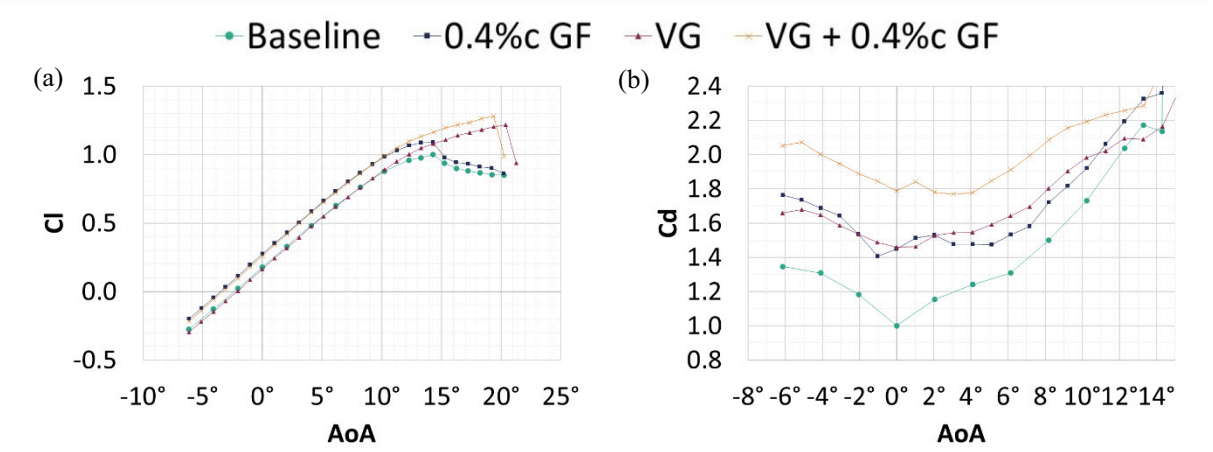

Figure 10. (a) Lift and (b) drag coefficient variation with AoA for the baseline airfoil, 0.4%c GF, VG, and VG + 0.4%c GF combination under free transition conditions. Wind Tunnel data at $Re = 10^6$, normalised results.

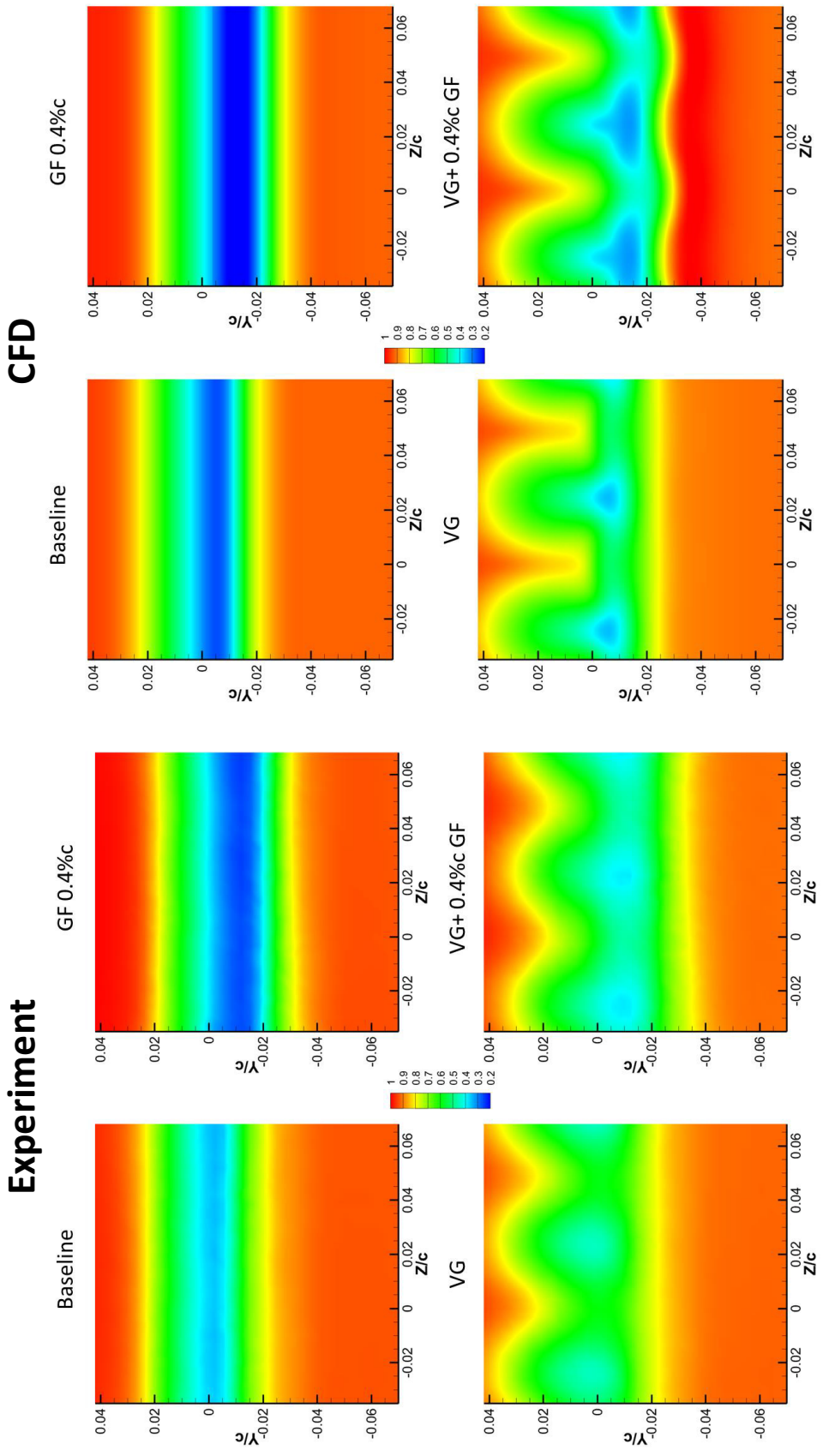

Figure 11. Normalised velocity magnitude contours on a plane normal to the flow, 5.8%c downstream of the trailing edge for the baseline airfoil, 0.4%c GF, VG, and VG + 0.4%c GF combination under fixed transition conditions, at $Re = 10^6$. The airfoil trailing edge is at Y/c=0, while Z/c=0 is a line between two VG pairs. Comparison of Stereo PIV measurements with CFD simulations.

4 Conclusions

To the best of authors' knowledge this is the first study of the complex interaction between VGs and GFs in the wake of an airfoil. The combination of VGs and GFs is successful in improving the L/D performance proving to counteract the negative effects caused by fixing LE transition. An increase of 23.4% in maximum L/D has been found for the combination of VGs with the smallest GF of 0.4 %c. For the VGs alone an increase of 20.8% was observed while for the GF (only) the increase in L/D (max) was 6.5%. VGs delay the formation of Stall Cells and hence the presence of bifurcating flows. GFs increase the amplitude of pressure changes, as they increase the difference in lift between stalled and non-stalled conditions. The interaction of the two devices in terms of drag appears to be linear for the free transition case, where the boundary layer thickness is smaller. On the other hand, in the fixed transition case, the linear drag increase cannot be reproduced in the combined case. URANS simulations were used to further analyse the flow interaction under examination. The simulations successfully predict the effect of each device on lift and drag, but the prediction of the combined effect is not equally good, possibly due to the non-linear interaction of the two control mechanisms. Finally, the wake flow past the two passive flow control devices was investigated by means of PIV measurements. It appears that the two effects (VGs + GF) are combined in the near wake of the airfoil. Again, CFD predictions are in good agreement with the wind tunnel measurements. Based on the presented results, combining relatively small VGs with GFs appears to have beneficial aerodynamic effects on the airfoil performance.

5 Acknowledgments

This research was funded by the EPSRC Impact Acceleration Account 2020 Research Impact Fund.
Computational resources were provided by Supercomputing Wales, which is gratefully acknowledged.

6 References

[1] Manolesos M, Voutsinas SG. Experimental investigation of the flow past passive vortex generators on an airfoil experiencing three-dimensional separation. J Wind Eng Ind Aerodyn 2015;142:130–48. https://doi.org/10.1016/j.jweia.2015.03.020

[2] Manolesos M, Papadakis G, Voutsinas SG. Assessment of the CFD capabilities to predict aerodynamic flows in presence of VG arrays. J Phys Conf Ser 2014;524:012029. https://doi.org/10.1088/1742-6596/524/1/012029.

[3] Soto-Valle R, Bartholomay S, Nayeri CN, Paschereit CO, Manolesos M. Airfoil Shaped Vortex Generators applied on a Research Wind Turbine. AIAA Scitech 2021 Forum, Reston, Virginia: American Institute of Aeronautics and Astronautics; 2021, p. 1413. https://doi.org/10.2514/6.2021-1413

[4] Manolesos M, Papadakis G, Voutsinas SGG. Revisiting the assumptions and implementation details of the BAY model for vortex generator flows. Renew Energy 2020;146:1249–61. https://doi.org/10.1016/j.renene.2019.07.063.

[5] Alber, J., Manolesos, M., Weinzierl-Dlugosch, G., Fischer, J., Schönmeier, A., Nayeri, C. N., Paschereit, C. O., Twele, J., Fortmann, J., Melani, P. F., and Bianchini, A.: Experimental investigation of Mini Gurney Flaps in combination with vortex generators for improved wind turbine blade performance, Wind Energ. Sci. Discuss. https://doi.org/10.5194/wes-2021-124, in review, 2021.

[6] Alber J, Soto-Valle R, Manolesos M, Bartholomay S, Nayeri CN, Schönlau M, et al. Aerodynamic effects of Gurney flaps on the rotor blades of a research wind turbine. Wind Energy Sci 2020;5:1645–62. https://doi.org/10.5194/wes-5-1645-2020

[7] Alber J, Pechlivanoglou G, Paschereit CO. Parametric Investigation of Gurney Flaps for the Use on Wind Turbine Blades. ASME Turbo Expo, Charlotte, NC: American Society of Mechanical Engineers; 2017, p. GT2017-64475. https://doi.org/10.1115/GT2017-64475

[8] Storms BL, Jang CS. Lift enhancement of an airfoil using a Gurney flap and vortex generators. J Aircr 1994;31:542–7. https://doi.org/10.2514/3.46528.

[9] Barlow JB, Rae WH, Pope A. Low-speed wind tunnel testing. New York: John Wiley & Sons; 1999.

[10] Kaufmann N, Carolus TH, Starzmann R. An enhanced and validated performance and cavitation prediction model for horizontal axis tidal turbines. International Journal of Marine Energy. 2017; 19:145–63. https://doi.org/10.1016/j.ijome.2017.07.003

[11] Ch'ng L. Using Vortex Generators and Gurney Flaps for Tidal Turbine Performance. MSc Thesis, Cranfield University, 2021.

[12] Drela M. XFOIL: An Analysis and Design System for Low Reynolds Number Airfoils. In: Mueller TJ, editor. Low Reynolds Number Aerodyn., vol. 54, NY, US: Springer-Verlag; 1989, p. 1–12.

[13] Papadakis G. Development of a hybrid compressible vortex particle method and application to external problems including helicopter flows. PhD Thesis, National Technical University of Athens, 2014.
[14] Chorin AJ. A numerical method for solving incompressible viscous flow problems. J Comput Phys 1967. https://doi.org/10.1016/0021-9991(67)90037-X
[15] Hejranfar K, Kamali-Moghadam R. Assessment of three preconditioning schemes for solution of the two-dimensional Euler equations at low Mach number flows. Int J Numer Methods Eng 2012. https://doi.org/10.1002/nme.3230
[16] Roe PL. Approximate Riemann solvers, parameter vectors, and difference schemes. J Comput Phys 1981;43:357–72. https://doi.org/10.1016/0021-9991(81)90128-5
[17] Venkatakrishnan V. On the Accuracy of Limiters and Convergence to Steady State Solutions. AIAA Pap., American Institute of Aeronautics and Astronautics (AIAA); 1993. https://doi.org/10.2514/6.1993-880
[18] Spalart P, Allmaras S. A one-equation turbulence model for aerodynamic flows. 30th Aerosp. Sci. Meet. Exhib., Reno, NV: American Institute of Aeronautics and Astronautics; 1992, p. 5–21. https://doi.org/10.2514/6.1992-439
[19] Menter FR. Two-equation eddy-viscosity turbulence models for engineering applications. AIAA J 1994;32:1598–605. https://doi.org/10.2514/3.12149
[20] Jirasek A. Vortex-Generator Model and Its Application to Flow Control. J Aircr 2005;42:1486–91. https://doi.org/10.2514/1.12220.
[21] Broeren AP, Bragg MB. Spanwise variation in the unsteady stalling flowfields of two-dimensional airfoil models. AIAA Journal. 2001;39(9):1641–51. https://doi.org/10.2514/2.1501
[22] Manolesos M, Voutsinas SG. Geometrical characterization of stall cells on rectangular wings. Wind Energy 2013; 17(9):1301–14. http://doi.wiley.com/10.1002/we.1634
[23] Kamenetskiy DS, Bussoletti JE, Hilmes CL, Venkatakrishnan V, Wigton LB, Johnson FT. Numerical Evidence of Multiple Solutions for the Reynolds-Averaged Navier–Stokes Equations. AIAA Journal 2014;52(8):1686–98. http://dx.doi.org/10.2514/1.J052676
[24] Baldacchino D, Ferreira C, Tavernier D de, Timmer WA, van Bussel GJW. Experimental parameter study for passive vortex generators on a 30% thick airfoil. Wind Energy 2018; 21(9):745–65. http://doi.wiley.com/10.1002/we.2191
[25] Manolesos M, Papadakis G, Voutsinas SG. Experimental and computational analysis of stall cells on rectangular wings. Wind Energy 2014;17(6):939–55. http://doi.wiley.com/10.1002/we.1609
[26] Manolesos M, Papadakis G. Investigation of the three-dimensional flow past a flatback wind turbine airfoil at high angles of attack. Physics of Fluids 2021;33(8):085106. https://aip.scitation.org/doi/abs/10.1063/5.0055822